ACS APPLIED NANO MATERIALS

Open Access

This article is licensed under CC-BY 4.0

www.acsanm.org

Article

Focused Electron Beam-Induced Deposition of Oblique Co and Fe Nanowires: Compositional and Magnetic Characterisation for Functional 3D Nanostructures

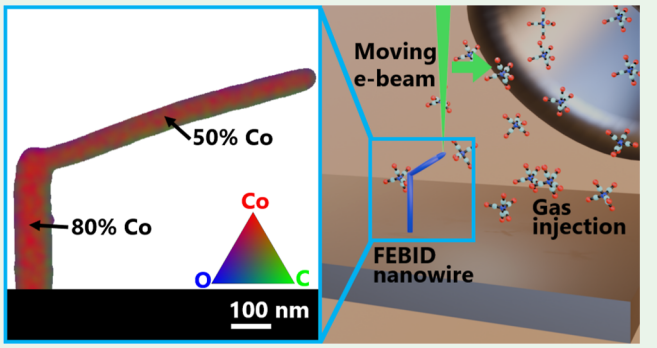
Aurys Šilinga,* Keir L. Edgar, András Kovács, Stephen McVitie, Rafal E. Dunin-Borkowski, Kayla Fallon, and Trevor P. Almeida*

Cite This: *ACS Appl. Nano Mater.* 2026, 9, 19185–19197

Read Online

ACCESS | Metrics & More | Article Recommendations | Supporting Information

ABSTRACT: Focused electron beam induced deposition (FEBID) is an additive manufacturing technique uniquely suited for fabricating functional 3D nanostructures for a range of applications, including spintronic devices. However, the variation of growth dynamics associated with lateral movement of the electron beam results in structures with non-uniform composition when fabricating intricate 3D geometries. Herein, we measure changes in atomic composition and corresponding changes in magnetic induction in 3D ferromagnetic nanostructures with overhanging elements, e.g. bridges or arches. To investigate the effects of electron beam lateral movement, we fabricated Co and Fe nanowire (NW) structures with growth angle relative to the optic axis varying from 0° to 90°. The (scanning) transmission electron microscopy techniques of electron energy loss spectroscopy and off-axis electron holography were performed to map the NW elemental composition and magnetic induction as a function of NW growth angle. Comparison of the results reveals a reduction in metal content with increased growth angle in FEBID NWs. The magnitude of metal content reduction can be tuned by controlling electron beam parameters, and ferromagnetic NWs with approximately equal metal content at growth angles from 0° to 60° were fabricated by using the lowest viable electron beam voltage and the highest viable beam current to reduce the interaction volume and increase the metal content, respectively.



KEYWORDS: *nanostructure, ferromagnetism, FEBID, electron microscopy, electron holography, 3D, fabrication*

INTRODUCTION

The environmental impact of conventional electronics can be mitigated by the development of spintronic computing architectures, which are theoretically more energy-efficient when handling digital data.[1] Devices including magnetic racetrack memory for data storage[2] or magnetic synapses for artificial neural networks[3] function by moving and storing data as magnetic domain walls in ferromagnetic nanowires (NWs). These designs have been tested in two-dimensional (2D) racetracks,[2] but by expanding to three-dimensional (3D) architectures, the component density per chip area can be increased by angling NWs vertically with respect to the substrate.[4] Additionally, the shape anisotropy and symmetry breaking induced by NW curvature[5,6] can be used to tune magnetic interactions that control magnetic domain wall (DW) movement. Complex 3D NW structures can be fabricated using focused electron beam induced deposition (FEBID), which is an additive manufacturing technique that can locally deposit ferromagnetic NWs with diameters down to 50 nm.[7,8] Even though the range of fabrication geometries is generally as unlimited as 3D-printing,[9] many functional ferromagnetic structures comprise NWs that are deposited at a constant angle to the substrate.[7,10] Since the purity and magnetic properties of the FEBID material are generally dependent on the orientation of the electron beam,[11] movement of the beam can cause composition variations in the deposited nanostructures.[9] Ensuring that functional FEBID nanostructures have a uniform composition when fabricating complex geometries is crucial for the design of magnetic devices, therefore, deposition parameters are tested.

FEBID Chemical Reactions

FEBID is performed by injecting a precursor gas into the sample chamber of a scanning electron microscope (SEM) and irradiating solid material with the electron beam.[7,11] This process drives the dissociation of precursor gas molecules primarily through irradiation

Received: May 29, 2026
Revised: September 10, 2026
Accepted: September 11, 2026
Published: October 5, 2026



ACS Publications

© 2026 The Authors. Published by American Chemical Society

Downloaded from pubs.acs.org/aanm6/article-pdf/9/41/19185/6874537/an6c02497.pdf by FORSCHUNGSZENTRUM JUELICH user on 16 October 2026

by secondary electrons (SEs) emitted from the substrate, and other forms of radiation present in the vicinity of the beam. The reaction products deposit on surfaces in the vicinity of the reaction volume, typically forming a deposit of nanocrystalline or amorphous metal. The primary challenge associated with FEBID is fabricating nanostructures with desired geometries while maintaining high metal purity, e.g., Co, Fe, etc. Inclusion of C & O contaminants and incomplete dissociation of the precursor gas is inherent to the FEBID process, which can result in relatively low metallic content [12] and loss of ferromagnetic properties. Optimising the deposition parameters and inclusion of post-processing stages have been thoroughly investigated to produce deposits with predictable ferromagnetic and charge transport behaviours, required for reliable device operation.[13−15] The composition of FEBID material is attributed to the balance between multiple chemical reactions occurring at the site where the electron beam is incident on a substrate.[12] This includes adsorption, which involves the formation of a bond between the precursor gas and the substrate; dissociation of the precursor molecules via bond cleavage; and the desorption of reaction products from the surface. The underlying chemical reactions have been studied both in isolation and as a combined deposition reaction. Co and Fe deposition is discussed in this work.

For the commonly used $Co_2(CO)_8$ precursor gas, autocatalytic adsorption has been observed to occur spontaneously,[16] but can also be driven by electron impact (EI) ionisation.[12,17] Regarding dissociation, mass spectroscopy experiments have shown that EI most frequently breaks bonds between Co and organic ligands, resulting in the creation of ions of the form $Co_2(CO)_8 \rightarrow Co_{1-2}(CO)_{0-8}^{\pm}$.[17] Calorimetry experiments have also shown that thermal dissociation (TD) at temperatures above 80 °C results in the deposition of pure Co and the desorption of CO gas, $Co_2(CO)_8 \rightarrow^{80^\circ} 2Co\downarrow + 8CO\uparrow$.[18] Although the FEBID material can contain organic ligands and is not guaranteed to be ferromagnetic, the conventional beam−matter interactions of ionisation by scattered electrons and beam-induced heating act to increase the metal content, which can be tuned by controlling the electron beam.[13]

For comparison, the $Fe_2(CO)_9$ precursor gas also undergoes EI ionisation of the form $Fe_2(CO)_9 \rightarrow Fe_{1-2}(CO)_{0-9}^{\pm}$,[19] and TD $Fe_2(CO)_9 \rightarrow^{280^\circ} 2Fe\downarrow + 9CO\uparrow$ above 280 °C.[18] Additionally, when $Fe_2(CO)_9$ is exposed to white light, heat, or electron beams,[20] it partially converts to $Fe(CO)_5$, which adsorbs autocatalytically.[21] In practice, the deposition process for Fe and Co precursors is similar, but the higher TD temperature for $Fe_2(CO)_9$ requires the use of a higher intensity electron beam to promote TD when depositing Fe NWs.

Experimentally, when the electron beam in an SEM is stationary or rastering over a flat substrate, the elemental composition, magnetisation, electrical resistivity, and geometry of the deposited structure can be reproducibly controlled.[8] This is achieved by tuning several deposition parameters, including the SEM accelerating voltage, the beam current, the concentration of precursor gas, and the dwell time at each beam position. Using these methods, more than 90% metal content has been achieved regularly in planar films and straight pillars.[14,22,23] In comparison, when fabricating geometrically complex nanostructures, the position of the electron beam can be controlled precisely, but beam movement alters the radiation dose absorbed per unit volume during deposition. Maintaining the high irradiation required to break metal-carbon bonds and deposit high-purity ferromagnetic metal is not straightforward when the beam transmits through a 3D sample and induces codeposition on multiple surfaces. Therefore, a trade-off must be made between beam energy, which affects interaction volume, and beam current, which affects beam intensity.

The metal content of deposited NWs can be further improved by post-growth treatments, which include thermal annealing, electron beam curing, reactive gas exposure, and combinations of each.[14,24,25] Thermal annealing has been the most extensively investigated and successful post-processing treatment for increasing the relative metallic content in FEBID deposits. Annealing temperatures in the 300−600 °C range are observed to induce thermal dissociation of carbonaceous material, which can diffuse and desorb from the deposit surface.[11,26] This has been studied with Co[27,28] and Fe[29,30] precursors, resulting in enhanced purity and crystallinity of FEBID deposits for most tested nanostructure geometries. Overall, FEBID of vertical NWs and flat films has been extensively studied to tune material functional properties, but FEBID material composition in oblique NWs is geometry-dependent and should be characterised to inform the fabrication of bespoke 3D nanostructures.

FEBID 3D Printing

The electron beam in an SEM can be programmed to move laterally along a predefined path, which results in NWs growing at an angle (θ) relative to the beam-axis, as illustrated in Figure 1a. $\theta = 0^\circ$ corresponds to a NW that is deposited around a stationary electron beam, and, in this work, is approximately perpendicular to the substrate surface (vertical). A laterally moving beam can be used to fabricate intricate 3D NW structures, such as double-helices, helical lattices, Moebius strips, or NW cubes that show curvilinear magnetic interactions,[9,31,32] and may inform the design of spintronic devices. To fabricate such 3D nanostructures, predictive models are used to generate stream files that control the lateral movement and dwell time of the incident electron beam. Models based on Langmuir-type approaches[33,34] or atomistic Monte-Carlocalculations[35,36] have been developed to enable FEBID 3D printing from CAD designs and fabrication of micrometre-sized FEBID structures from Co or Fe. These model types assume that material is deposited in thin layers without affecting the layers underneath, which does not account for TD occurring in all of the volume heated by the beam and does not predict either anisotropic growth of oblique NWs[9] or auto-catalysed crystalline growth.[21] Such models are most accurate when TD is limited, and hence lower-purity material is deposited. Methods have been developed to simulate thermal conductance and FEBID TD reactions,[9,37] but they have only been tested so far with Pt and Au.

In practice, the material properties of FEBID NWs are tuned depending on the intended application. Such optimisations leverage the observation that NWs exhibit characteristic responses to changes in deposition parameters.[13] Since FEBID precursor gases for Co and Fe are chemically similar and the underlying electron scattering interactions are the same,[38] the effects of changing deposition parameters are also similar. They can be observed by depositing two NWs side-by-side; starting with NW "A", changing one deposition parameter, and then depositing NW "B". The observed characteristic effects are:

E0. When nothing is changed, A and B are approximately identical. This indicates that the deposition is consistent, and is a necessary condition for the accuracy of FEBID CAD modelling.[9,33,35]

Downloaded from pubs.acs.org/aanm6/article-pdf/9/41/19185/6874537/an6c02497.pdf by FORSCHUNGSZENTRUM JUELICH user on 16 October 2026

https://doi.org/10.1021/acsanm.6c02497
ACS Appl. Nano Mater. 2026, 9, 19185−19197

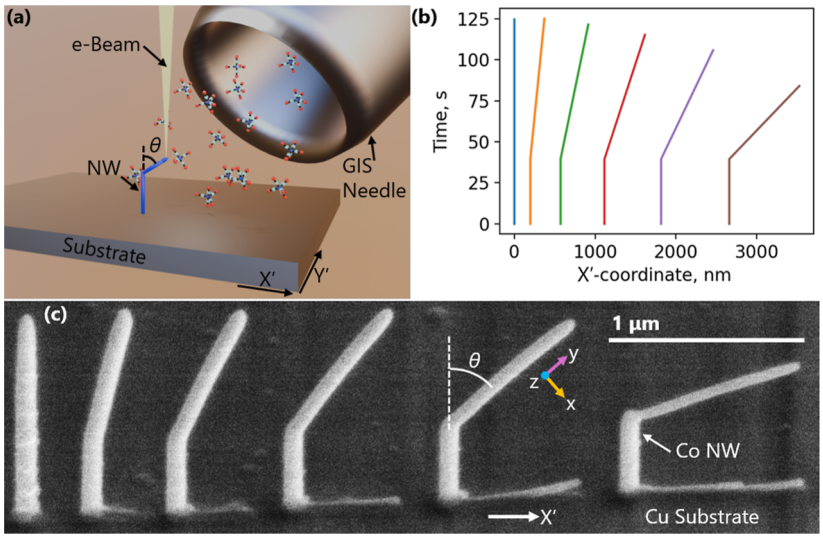


Figure 1. FEBID 3D printing process. (a) Schematic diagram of FEBID process, where NW structures are fabricated by injecting precursor gas through the GIS needle and laterally moving the electron beam along a path defined by stream files in SEM. (b) Streams that define beam position as a function of time, during deposition. (c) Tilt-corrected SE SEM image of FEBID Co NWs fabricated by executing the streams in (b). The inset shows the sample-aligned coordinate system used later in the analysis. To fabricate oblique nanostructures (c), the beam must be stationary at each position for an amount of time corresponding to (b).

E1. When the beam current is increased, B will have a larger volume and higher metal content than A, as demonstrated for Co and Fe.[15,22,39] There is an upper limit to the beam current beyond which randomly oriented crystalline growth is observed.[20,21,40,41]

E2. When the beam is defocused, B will have a larger diameter and lower metal content than A. This has been observed for Co, Fe, and Pt[13,38,42,43]

E3. When B is annealed at a temperature in the 300−600 °C range, its metal content will increase, as seen for both Co and Fe.[27−30]

E4. When the beam accelerating voltage is increased, the geometry of B will be different from A. If the SEM beam is moving laterally during deposition, then the cross-section of B will be more elongated (elliptical) than the cross-section of A. This has been observed for Fe, Co, $FeCo_3$, and Pt.[9,10,21,43,44]

E5. If the lateral movement speed of the beam is increased, the metal content of B will decrease relative to A. This is measured for Co and Fe NWs in this work.

In this work, Co NWs are fabricated with $\theta = 0°$ to test effects E0-E3 and verify that the FEBID system is functioning normally. Then Co NWs and Fe NWs are fabricated with $0° \leq \theta < 90°$ at different accelerating voltages to quantify effects E4 & E5 and test whether E5 is material-agnostic. Furthermore, correlations among θ, metal content, and magnetic induction in ferromagnetic NWs are measured; to develop methods for improving oblique NW composition uniformity and inform the development of FEBID 3D-printing algorithms for ferromagnetic nanostructures.

METHODS

Sample Fabrication

A dual-beam Thermo Fisher Scientific HELIOS Xe plasma focused ion beam (FIB) SEM was used to ion-mill flat substrates from a copper film, which could be electrically grounded during TEM and SEM imaging. NWs were deposited on the copper substrates using FEBID. The gas injection system (GIS) heated solid precursor material to induce sublimation, and the precursor gas was injected through the GIS needles positioned at an approximately 250 μm height above the substrate surface and a 100 μm lateral distance from the deposition point. Co and Fe needles were inserted at 40° and 60° angles relative to the SEM beam, respectively. The needle orientation in the lateral plane was at a 50° angle clockwise from the $+X'$ direction. For FEBID, the $Co_2(CO)_8$ and $Fe_2(CO)_9$ precursors were heated to 29 °C and 37 °C, respectively. Nine sets of FEBID NWs were fabricated: first, five sets to characterise NWs deposited using a stationary electron beam as reference samples; and secondly, another four sets to measure the composition change in NWs deposited with a laterally moving electron beam. Table 1 lists the details of each sample set, including the precursor gas, beam accelerating voltage and current. For completeness, the base pressure in the SEM chamber was recorded before and during deposition, and to indicate the reaction rate, the vertical NW height to deposition time ratio (growth rate) is recorded. Compositional analyses and beam conditions for each individual NW are provided in the Supporting Information.[1] The arrows in the dataset titles indicate whether the deposition was at $\theta = 0°$ (↑) or $\theta > 0°$ (↗). All NWs were deposited sequentially, from left to right. For each deposition, the electron beam was focused to achieve minimum NW diameter. The samples were plasma-cleaned with an oxygen-argon 1:3 mixture for 15 s to reduce amorphous carbon growth during scanning TEM (STEM) imaging. Calibration EELS measurements showed that 15 s of plasma-cleaning removed an approximately 5 nm thick layer from the carbon-rich Co NW surface and changed the number of O and Co atoms by less than 1%.

The NW structures were fabricated using stream files that encode the beam's X'- and Y'-deflections (in the substrate plane) as functions of deposition time. Vertical NWs were deposited using a stationary beam for 120 s, whilst oblique NWs were deposited by keeping the beam stationary for 40 s and then moving it laterally in the X′-direction at a constant rate for up to 80 s. The stream files were generated using the F3ast software package[9] and were calibrated to increase X'-deflection in approximately 2.5 nm steps at rates from 0 to 8 steps per second. The electron beam dwell time at each coordinate is shown in Figure 1b. For the $\mathbf{Co}^{\nearrow}_{5kV}$ dataset, each stream in Figure 1b moves the SEM beam at a different rate; therefore, the deposited NWs in Figure 1c grow at different angles relative to the vertical NW. Samples from all datasets

Downloaded from pubs.acs.org/aanmf6/article-pdf/9/41/19185/6874537/an6c02497.pdf by FORSCHUNGSZENTRUM JUELICH user on 16 October 2026

https://doi.org/10.1021/acsanm.6c02497
ACS Appl. Nano Mater. 2026, 9, 19185−19197

Table 1. Deposition Parameters for FEBID Samples[a]

dataset title	beam voltage (kV)	beam current (pA)	deposition pressure (Pa)	base pressure (Pa)	growth rate (nm/s)	precursor gas
$\mathbf{Co}_{\mathbf{anneal,30kV}\uparrow}$	30	21 − 340	0.9×10^{-4}	0.5×10^{-4}	6−10	$Co_2(CO)_8$
$\mathbf{Co}_{\mathbf{30kV}\uparrow}$	30	170 − 2800	2.2×10^{-4}	0.7×10^{-4}	8−26	$Co_2(CO)_8$
$\mathbf{Co}_{\mathbf{5kV}\uparrow}$	5	170 − 2800	2.2×10^{-4}	0.7×10^{-4}	11−22	$Co_2(CO)_8$
$\mathbf{Fe}_{\mathbf{30kV}\uparrow}$	30	170 − 11000	1.5×10^{-4}	0.2×10^{-4}	6−20	$Fe_2(CO)_9$
$\mathbf{Fe}_{\mathbf{5kV}\uparrow}$	5	170 − 11000	$1.2 \cdot 10^{-4}$	0.2×10^{-4}	6−20	$Fe_2(CO)_9$
$\mathbf{Co}_{\mathbf{30kV}\nearrow}$	30	690	2.2×10^{-4}	0.7×10^{-4}	8	$Co_2(CO)_8$
$\mathbf{Co}_{\mathbf{5kV}\nearrow}$	5	340	2.2×10^{-4}	0.7×10^{-4}	11	$Co_2(CO)_8$
$\mathbf{Fe}_{\mathbf{30kV}\nearrow}$	30	2800	0.8×10^{-4}	0.2×10^{-4}	5	$Fe_2(CO)_9$
$\mathbf{Fe}_{\mathbf{5kV}\nearrow}$	5	2800	1.0×10^{-4}	0.2×10^{-4}	7	$Fe_2(CO)_9$

[a]Each dataset corresponds to a series of NWs deposited by executing the stream files in one area of the sample.

are shown in Figure 2. Datasets $\mathbf{Co}^{\uparrow}_{30kV}$, $\mathbf{Co}^{\uparrow}_{5kV}$, $\mathbf{Co}^{\uparrow}_{anneal,30kV}$, $\mathbf{Fe}^{\uparrow}_{30kV}$, and $\mathbf{Fe}^{\uparrow}_{5kV}$ are used to find deposition parameters that enable controlled deposition of vertical ferromagnetic NWs. Datasets $\mathbf{Co}^{\nearrow}_{5kV}$, $\mathbf{Co}^{\nearrow}_{30kV}$, $\mathbf{Fe}^{\nearrow}_{5kV}$, and $\mathbf{Fe}^{\nearrow}_{30kV}$ use the parameters that deposit ferromagnetic material to fabricate oblique NW structures. For calibration, NWs in the dataset $\mathbf{Co}^{\uparrow}_{anneal,30kV}$ were fabricated with lower currents and gas pressures, and characterised before and after annealing at 350 °C for 30 min to verify consistency with previous works.[13,15,25,28] The NWs were annealed in situ at high vacuum using a Gatan 628 single-tilt TEM heating holder. In summary, stream files are defined to fabricate oblique FEBID NWs with growth angles ranging from 0° to 90°, and are executed using different precursor materials, accelerating voltages, and beam currents.

The precursor gas pressure was held constant during stream file execution, with fluctuations not exceeding 2×10^{-5} Pa, which accounts for pressure changes of less than 15% and is assumed to have negligible effects on composition or growth rate.[22] The spatial distribution of precursor gas concentration depends on GIS alignment[45] and can affect NW deposition reaction rate, geometry, and atomic composition.[22] Although local gas concentrations were not measured, they are assumed to be constant because GIS alignment and chamber pressure were constant during deposition.

Elemental Mapping

A JEOL ARM200cf operated at 200 kV (University of Glasgow) equipped with a cold field emission gun, a CEOS (Corrected Electron Optical Systems GmbH) probe corrector and a Gatan 965 Quantum ER spectrometer was used to perform STEM electron energy loss spectroscopy (EELS) elemental mapping. A dual EELS system with a high-speed electrostatic deflector[46,47] allowed for the simultaneous acquisition of high-loss and low-loss spectra from select areas of the FEBID NWs. The spectra were acquired using a 0.5 eV/pixel dispersion, 2.5 mm aperture, 29 mrad convergence semi-angle and 36 mrad collection semi-angle. Principal component analysis (PCA)[48] was utilised to remove X-ray signatures and reduce noise in high-loss spectra by reconstructing from the first 150 components, such that PCA would alter quantification results by less than 0.1% in sample areas with high signal-to-noise ratio (SNR), but provide smoothing in areas of low SNR. Spectra with more than 10^4 counts per energy channel in the fitting region were quantified using the Gatan Digital Micrograph elemental quantification plugin.[49] Supporting Information Figure S10 compares high-loss EELS spectra from 20 nm wide centre bands of NWs with 130 nm and 30 nm projected thicknesses, showing that sufficient EELS signal was acquired for all NWs. The measurement error stems from the combined contributions of Poisson noise and uncertainties of fitting Hartree-Slater cross sections.[50] The uncertainty for relative atomic content measurement (atom %) in the thickest parts of the NWs is less than 3% per scanned pixel.

A Cartesian coordinate system was defined to describe compositional distributions in oblique cylindrical NWs (Figure 1c inset), with the z-axis parallel to the TEM beam, the y-axis parallel to the NW length, and the x-axis parallel to the projected NW diameter. Figure 3 provides an example. The variation along the x-axis in the calculated EELS map Figure 3a corresponds to the projected distribution of atomic composition for a model NW with a radially varying composition and an elliptical cross-section, as shown in Figure 3b. FEBID NWs exhibit a radially layered structure, which is consistent with a Co (or Fe) rich core and an outer shell rich in C and O. Hence, care must be taken when interpreting EELS maps, as they represent the thickness projection of a radially varying structure, as previously observed.[51] This model is qualitatively consistent with experimental EELS maps of straight NWs with smooth surfaces. Such as the example shown in Figure 3c,e, deposited with a 340 pA beam current in the $\mathbf{Co}^{\uparrow}_{5kV}$ sample. However, one EELS map acquired in projection is insufficient to reconstruct the 3D distribution of atomic composition, thus, the core−shell structure is assumed based on cross-sectional measurements in previous works.[15] A quantitative model that consistently describes the internal composition of all FEBID NWs is not presented in this study, but plausible composition models for illustrative purposes are discussed in the Supporting Information.[2] In this analysis, the metallic atom content is measured as the average concentration of Co or Fe atoms in the centre band, corresponding to the volume indicated by dashed lines in Figure 3, defined as the 20 nm wide area around the projected centre of mass in the EELS compositional map. To enable comparison, measurements of magnetic induction will also consider only the average magnetic field within this volume.

Measurement of NW Elliptical Cross-Section Shape

The 3D sample geometry must be known to perform quantitative measurements of magnetic induction. Therefore, NW cross-sectional shapes are approximated by ellipses as shown in Figure 3b, with the semi-major and semi-minor axes of the ellipse labelled r_a & r_b, respectively. They define a cylinder in 3D space, with coordinates $z = r_b \cos(p)$; $x = r_a \sin(p)$. Where p is an arbitrary real-valued parameter and z & x are coordinates. When the sample is tilted by an angle γ during SEM imaging, it is equivalent to a rotation around the X′-axis of the SEM sample stage. Then, the observed NW width (W) is a tomographic projection[52] of the ellipse, given by the expression

$$W(\gamma) = 2\left(r_a \cos(p_m)\sin(\gamma) + r_b \sin(p_m)\cos(\gamma)\right). \quad (1)$$

where $p_m = \arctan\left(\frac{r_b \cos(\gamma)}{r_a \sin(\gamma)}\right)$ is the ellipse parameter corresponding to the point farthest from the origin in the projection plane. The axes can be measured by imaging the sample at $\gamma = 0°$ and $\gamma = 90°$, providing values of $W(0°) = 2r_b$ and $W(90°) = 2r_a$. When the model is accurate, W measurements at intermediate γ values are consistent with eq 1. In which case, the spatial variation of the projected NW thickness during TEM imaging is given by

$$t_z(x) = 2r_b\sqrt{1 - \left(\frac{x}{r_a}\right)^2}. \quad (2)$$

This is needed to measure spatially resolved magnetic induction ($\boldsymbol{B}(x)$). W measurements from both SEM and STEM were used to

Downloaded from pubs.acs.org/aanm6/article-pdf/9/41/19185/6874537/an6c02497.pdf by FORSCHUNGSZENTRUM JUELICH user on 16 October 2026

https://doi.org/10.1021/acsanm.6c02497
ACS Appl. Nano Mater. 2026, 9, 19185−19197

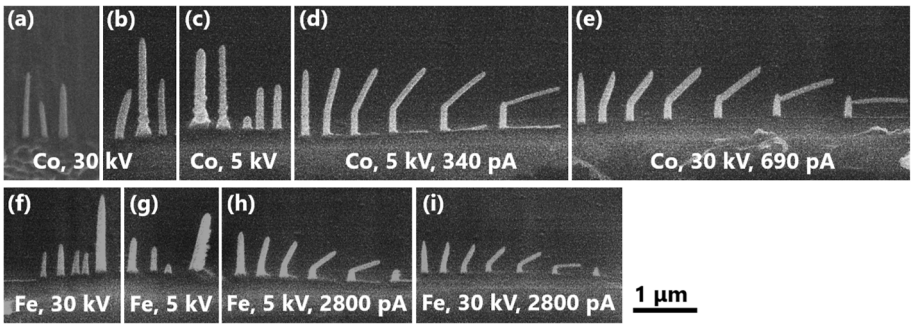


Figure 2. SE SEM images of FEBID NWs that are characterised and compared. (a) $\mathbf{Co}^{\uparrow}_{\mathbf{anneal},30kV}$. (b) $\mathbf{Co}^{\uparrow}_{30kV}$. (c) $\mathbf{Co}^{\uparrow}_{5kV}$. (d) $\mathbf{Co}^{\nearrow}_{5kV}$. (e) $\mathbf{Co}^{\nearrow}_{30kV}$. (f) $\mathbf{Fe}^{\uparrow}_{30kV}$. (g) $\mathbf{Fe}^{\uparrow}_{5kV}$.(h) $\mathbf{Fe}^{\nearrow}_{30kV}$. (i) $\mathbf{Fe}^{\nearrow}_{5kV}$. All images were acquired with the sample tilted by 55° and are shown at the same scale. High-resolution images and deposition parameters for each NW are available in the Supporting Information.[1]

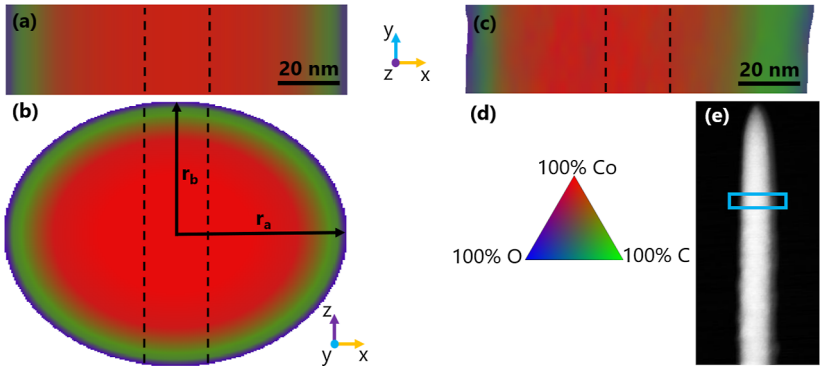


Figure 3. Assumed model of NW atomic composition. (a) Calculation of a compositional map, assuming the NW cross-section (b). (b) Model of an elliptical cross-section with a pure Co core, intermediate layers, and outer layers rich in C and O. (c) STEM EELS compositional map for a vertical NW in dataset $\mathbf{Co}^{\uparrow}_{5kV}$. (d) Colour map for (a–c). (e) STEM annular dark field (ADF) image identifying the location where (c) was acquired. FEBID NWs are modelled as multi-layered structures with elliptical cross-sections. Black arrows indicate the semi-axes of the ellipse, the insets show the coordinate system, and the dashed lines identify the volume where the composition was measured.

calculate t_z because this approach reduces uncertainty and ensures consistency between instruments. The SEM images were acquired using an SE detector and have a 2.2 nm pixel size. STEM images were acquired with 2 nm pixel size using either an ADF detector or the EELS spectrometer. For all NWs, the W(55°) measurements were within 5 nm of eq 1, which is equivalent to an r_b measurement error lower than 2 nm and is assumed to be consistent with the model. Uncertainties in r_a and r_b are assumed to be equal to the pixel size and were propagated in calculations of t_z and $\boldsymbol{B}$.

Magnetic Characterisation

Off-axis electron holography[53] is performed to reconstruct the magnetic phase shift (φ_m) of an electron wave passing through the sample and calculate $\boldsymbol{B}$. Electron holograms were acquired using an image aberration-corrected FEI Titan G2 60–300 TEM operated at 300 kV (Ernst Ruska-Centre for Microscopy and Spectroscopy with Electrons) in magnetic-field-free conditions (Lorentz mode). Images and electron holograms were recorded using a direct electron counting Gatan K2 detector. A 100 V voltage was applied to the electron biprism, resulting in a hologram fringe spacing of approximately 3 nm. The total phase shift (φ) was reconstructed using Holoworks[54] and Holoview[55] extensions for the Digital Micrograph Software package.[56] Maps of φ are reconstructed with 5 nm spatial resolution, determined by the size of the virtual aperture selecting the hologram sideband. The phase maps showed 0.01 rad noise corresponding to the root-mean-square (RMS) difference between two vacuum reference images. Since the z-axis is defined as being parallel to the TEM electron beam direction and the y-axis is parallel to the NW centreline, the Aharonov-Bohm effect[57] can be expressed as

$$\varphi = \varphi_{el}(V) + \varphi_m(A_z) = \frac{e}{\hbar v}\int V dz + \frac{e}{\hbar}\int A_z dz. \quad (3)$$

where φ_{el} and φ_m are the electrostatic and magnetic contributions to the total phase shift (φ), respectively, e is the charge of an electron, $\hbar$ is the reduced Planck constant, v is the relativistic electron speed, V is the electrostatic potential, A_z is the z-component of the magnetic vector potential, and dz is a path element along the z-axis. The integral is over the full trajectory of the beam. To separate φ_m from φ_{el}, the NWs are magnetically saturated by tilting the sample to large opposite ±70° α-tilt angles, applying a 1 T magnetic field using the objective lens of the microscope, and acquiring electron holograms at 0° α-tilt angle for the opposite remnant states. Assuming that the NW states after each saturation are equivalently opposite states of magnetisation ($\boldsymbol{M}$), the half-difference of the two φ maps corresponds to φ_m.[26] The $\boldsymbol{M}$ reversal is assumed to be complete because the φ gradient in vacuum around the NWs had changed sign and kept the same magnitude. Since $\boldsymbol{B}$ = curl($\boldsymbol{A}$), the thickness-averaged magnetic induction component parallel to the y-axis is given by

$$B_y(x) = -\frac{\hbar}{e\,t_z}\frac{d\varphi_m}{dx}. \quad (4)$$

where t_z is the NW thickness in projection along the z-axis, given by eq 2. The measurement of B_y is used to compare the strength of the magnetic induction fields created inside the NWs.

Downloaded from pubs.acs.org/aanmf6/article-pdf/9/41/19185/6874537/an6c02497.pdf by FORSCHUNGSZENTRUM JUELICH user on 16 October 2026

https://doi.org/10.1021/acsanm.6c02497
ACS Appl. Nano Mater. 2026, 9, 19185–19197

RESULTS

Comparison of Vertical NW Composition

To ensure consistency of analysis for all deposits, the vertical FEBID NW samples $\mathbf{Co}^{\uparrow}_{30kV}$ and $\mathbf{Co}^{\uparrow}_{\mathbf{anneal},30kV}$ (Figure 4a−c) provided a compositional reference. Figure 4d shows an EELS elemental map acquired from the blue square in Figure 4a and reveals the metallic core and carbonaceous shell of the NW, as seen in previous works.[15,28] In Figure 4e, the thickness-averaged cobalt content measured from the central 20 nm band (Figure 4d, rectangle) is compared to the other beam currents used for NWs in $\mathbf{Co}^{\uparrow}_{30kV}$, $\mathbf{Co}^{\uparrow}_{\mathbf{anneal},30kV}$, and $\mathbf{Co}^{\nearrow}_{30kV}$ samples. The systematic EELS fitting uncertainty is $<3\%$ for all points. In agreement with previous works, NWs with the highest metal content are deposited using higher beam currents and exhibit uneven surface topography.[16,20,28,39] Figure 4e also demonstrates that annealing the $\mathbf{Co}^{\uparrow}_{\mathbf{anneal},30kV}$ NWs at 350 °C for 30 min is an effective method of increasing the mean Co content, and correctly focusing the beam is important for depositing with high initial Co content.[14,25] Supporting Information[1] contains composition maps of all NWs, which are used for comparison in this subsection. It is assumed that the right side of the carbon-rich shell in Figure 4d is thicker primarily due to surface topography, as EELS maps acquired at a higher elevation along the NW indicate similar composition with reduced asymmetry. Furthermore, composition maps for vertical NWs deposited left-to-right with spacings from 300 nm to 500 nm do not show consistently increased shell thickness on the right side that might indicate codeposition induced by proximity effects.[58] In summary, the compositional analysis agrees with previous observations that the deposited metal content scales generally with electron beam current,[8] but high currents result in less consistent surface topologies.

Calibration of Oblique NW Shape and Composition Measurements

To enable comparison, all NWs are characterised using the same methods. Since the NW cross-sections can be elliptical, the NW diameter is measured twice by tilting the SEM stage and acquiring images at $\gamma = 0°$ and $\gamma = 55°$ tilt, as shown respectively in Figure 5a,b. The projected NW width is measured as the full-width at half-maximum (FWHM) of the intensity line profiles in the SEM images, as shown by the lines corresponding to $W(55°)$ and $2r_b$.

STEM EELS elemental maps are acquired with 2 nm resolution to characterise areas of interest, as shown in Figure 5c. The sample orientation during STEM imaging is equivalent to a $\gamma = 90°$ tilt, therefore the projected NW widths in the EELS maps can be used to determine r_a. Additionally, the radius of the calibration element (r) is the same in all projections, thus r measurements can be compared between SEM and STEM EELS. Based on an EELS thickness measurement, the SEM detects the NW edge at the position where the projected material thickness is 0.5 nm, which is significantly below the pixel size and does not require correction. Furthermore, the $W(55°)$ measurement is within two pixel-widths (5 nm) of eq 1, showing that the NW cross-sectional shape is consistent with an ellipse that has semi-axes r_a and r_b. Comparisons between NWs will be presented in a later section.

The deposition consistency is evaluated by ensuring that all nanostructures include a NW calibration element deposited with a stationary beam, such as the vertical sections shown in Figure 5b. EELS maps are used to compare the Co content in the calibration element, as shown in Figure 5d. The histograms of Co content measurements in the NW centre bands, corresponding to the rectangular boxes in Figure 5c, are shown by shaded areas between error bars (violin plots). The $\theta = 0°$ NW is the outlier, as the SEM beam is stationary, thus it transmits through the NW and irradiates the bottom layers for the entire deposition time. Consistent calibration sections indicate that the deposition parameters do not vary significantly across the nanostructures, enabling comparison of the oblique NW sections. The growth angle θ is defined relative to the SEM optical axis, as shown in Figure 5c. The Co content in the oblique NWs is compared in Figure 5e. This process is repeated to find correlations between metal content and θ in all oblique NW samples.

Correlation between Composition and Growth Angle

Having established fabrication and characterisation methods consistent with the expected results for vertical NWs, oblique NWs are characterised. Figure 6 presents the variation of NW composition and shape as a function of θ, for samples $\mathbf{Co}^{\nearrow}_{5kV}$, $\mathbf{Co}^{\nearrow}_{30kV}$, $\mathbf{Fe}^{\nearrow}_{5kV}$, and $\mathbf{Fe}^{\nearrow}_{30kV}$ (Figure 6a), which were fabricated by laterally moving the SEM beam during deposition. Figure 6b shows that the mean metal at. content (Co or Fe) in the 20 nm centre band decreases with increasing θ for all NWs. The average metal content loss per degree of growth angle is represented by the slope of a linear regression fit. It is $(0.11 \pm 0.05)\%/°$ for the $\mathbf{Fe}^{\nearrow}_{5kV}$ sample, $(0.20 \pm 0.02)\%/°$ for $\mathbf{Fe}^{\nearrow}_{30kV}$, $(0.41 \pm 0.04)\%/°$ for $\mathbf{Co}^{\nearrow}_{5kV}$, and $(0.45 \pm 0.05)\%/°$ for $\mathbf{Co}^{\nearrow}_{30kV}$. The length of r_a is shown in Figure 6c, revealing that the NW cross-sectional area shrinks during lateral beam movement. Figure 6d displays the r_a/r_b ratio as a function of θ, indicating that the NW cross-section becomes more elliptical if a 30 kV accelerating voltage is used and the beam is moved laterally, confirming previous works.[44] Comparison between r_a and r_b is shown in Supporting Information Figure S11, indicating that the minor axis also decreases as a function of θ. The results show that $\mathbf{Fe}^{\nearrow}_{5kV}$ maintains the highest metal content and the most circular cross-section shape when θ is increased. Additionally, Supporting Information Figure S12 shows a correlation between at. content measurement and NW cross-sectional area. Overall, $\mathbf{Fe}^{\nearrow}_{5kV}$ is the only dataset where θ, r_a, and metal at. content measurements are weakly correlated.

Micromagnetic Simulations of Cylindrical FEBID NWs

The micromagnetic simulations were performed using Mumax3[59,60] to determine $\boldsymbol{M}$ configurations that are energetically stable in cylindrical FEBID NWs comprising nanocrystalline or amorphous impure Co. To qualitatively evaluate possible $\boldsymbol{M}$ configurations, FEBID NWs can be approximated as uniform cylinders.[31,61] The exchange stiffness is $A_{ex} = 1.5 \times 10^{-11}$ J/m and the saturation magnetisation is $M_s = 8 \times 10^5$ A/m, based on previous FEBID simulations[31] and measurements of Co samples of different purities.[28,61,62] The simulation parameters for nanocrystalline impure Fe are similar[63] and produce equivalent results. A cubic mesh with 2.5 nm voxel size is used for an exchange length $l_{ex} = \sqrt{\frac{2A_{ex}}{\mu_0 M_s^2}} \approx 6$ nm.

To investigate magnetic configurations in FEBID NWs, 1 μm long cylinders of Co and Fe are simulated using micromagnetics. The diameters are varied in the range from 60 nm to 240 nm,

Downloaded from pubs.acs.org/aanm6/article-pdf/9/41/19185/6874537/an6c02497.pdf by FORSCHUNGSZENTRUM JUELICH user on 16 October 2026

https://doi.org/10.1021/acsanm.6c02497
ACS Appl. Nano Mater. 2026, 9, 19185−19197

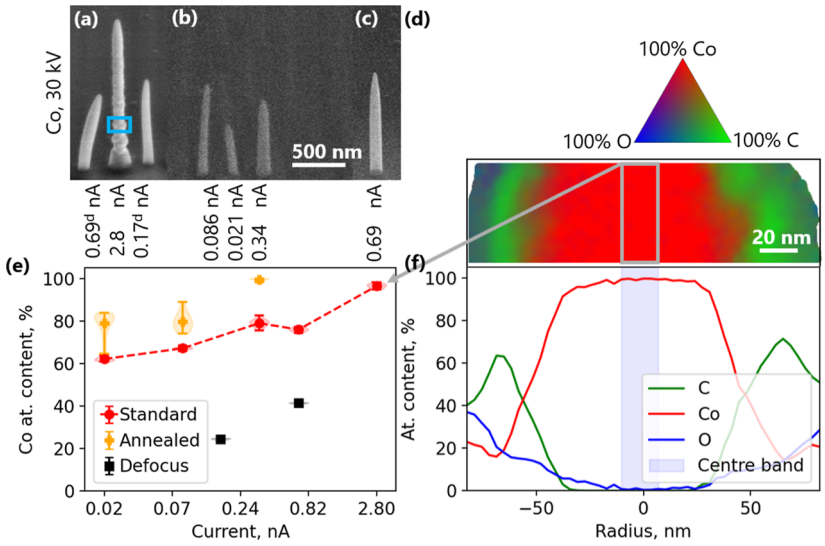


Figure 4. Comparison of vertical Co FEBID NWs deposited at 30 kV. (a-c) Vertical NWs from samples $\mathbf{Co}^{\uparrow}_{30kV}$, $\mathbf{Co}^{\uparrow}_{\mathbf{anneal},30kV}$, and $\mathbf{Co}^{\nearrow}_{30kV}$, respectively. The scale is identical in all three images, annotations show the beam current during deposition, and the [d] superscript identifies when the SEM beam was defocused. (d) EELS atomic composition map of the NW section corresponding to the blue box in (a). (e) Atomic Co content (%) in the NWs that are as deposited (standard), annealed, or deposited with a defocused beam. The error bars represent the range of Co content values measured in the centre band, and the violin plots represent the value histograms. The systematic uncertainty is 3%. The abscissa scale is $\log_2$. (f) Horizontal line-trace through (d), showing atomic content of all elements and the width of the centre band.

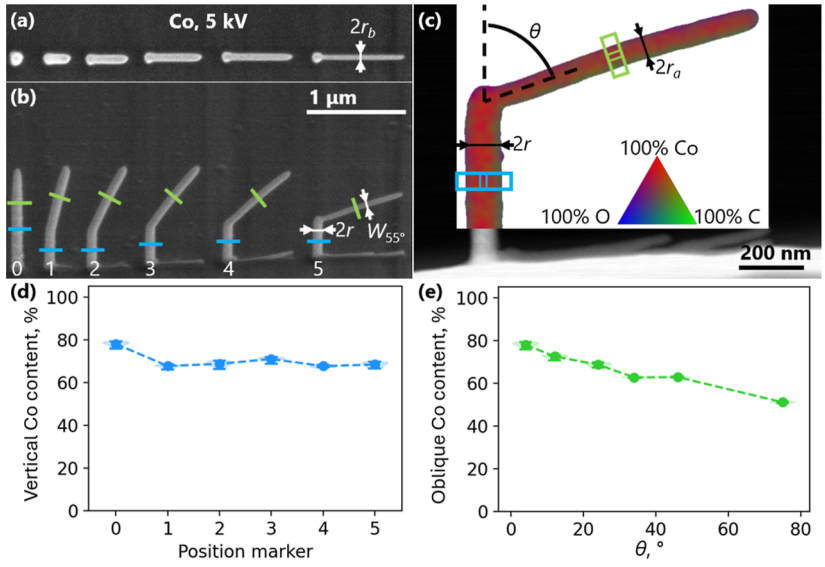


Figure 5. Measurement of cross-section shape and Co content for the $\mathbf{Co}^{\nearrow}_{5kV}$ sample. (a) 0° and (b) 55° tilt SEM images of NWs, respectively. The lines indicate the locations of high-resolution STEM EELS scans. (c) STEM EELS map displayed over a STEM ADF map of NW No. 5. The boxes indicate the locations of high-resolution STEM EELS scans, θ is the NW growth angle, and black lines correspond to width measurements relating to eq 1. (d) Co content in NW regions corresponding to the horizontal blue lines in (b), used to verify consistency. (e) Co content in NW regions corresponding to the angled green lines in (b).

and the initial $\boldsymbol{M}$ states are aligned parallel to the y-axis (magenta arrow in Figure 1), such that the simulation emulates a relaxation after being subject to a saturating external field.[60] Corresponding energetically stable configurations are shown in Supporting Information Figure S13. Whilst magnetic flux closure is always visible at the cylinder ends, the majority of the volume is magnetised parallel to the long axis if the cylinder diameter is below 160 nm. For diameters above 160 nm, various vortex configurations are observed. Micromagnetic simulations of NWs with elongated cross-sections corresponding to geometries in the experimental dataset show that oblique NWs are also predominantly magnetised parallel to the long axis. The $\boldsymbol{M}$ configuration corresponding to the most elliptical NW with r_a = 62.5 nm and r_b = 25 nm is shown in the Supporting Information Figure S14. Based on these simulations, the oblique NWs in Figure 6 are expected to be uniformly magnetised. Hence, simulations show that the thickness-average of B_y calculated from φ_m using eq 4 corresponds to the average magnitude of $\boldsymbol{B}$.

The recorded B_y values represent a measurement of average $\boldsymbol{B}$ magnitude in volumes where the demagnetising field is non-negligible, and the NW material comprises both ferromagnetic and paramagnetic regions. However, since the NWs are

https://doi.org/10.1021/acsanm.6c02497
ACS Appl. Nano Mater. 2026, 9, 19185−19197

Downloaded from pubs.acs.org/aanmf6/article-pdf/9/41/19185/6874537/an6c02497.pdf by FORSCHUNGSZENTRUM JUELICH user on 16 October 2026

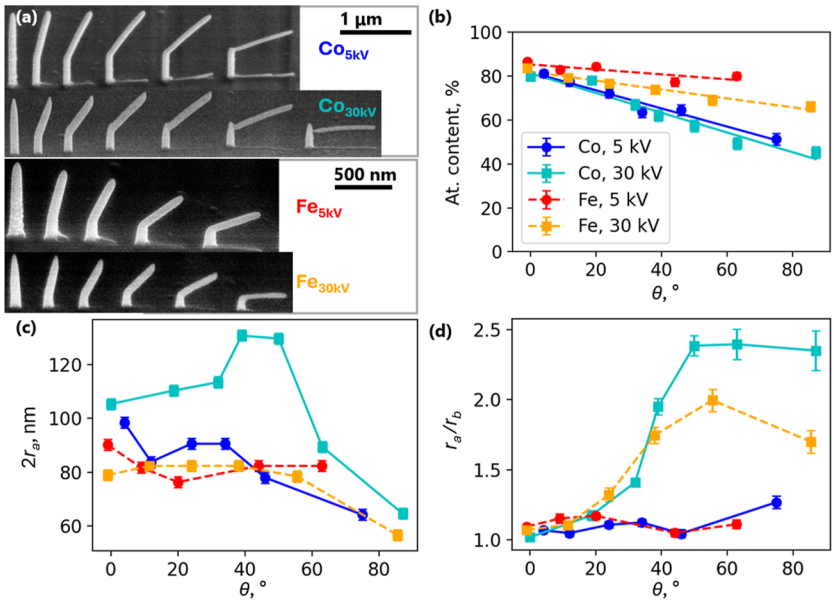


Figure 6. Variation in oblique NW composition and shape as a function of growth angle. (a) SE SEM images of the $\mathbf{Co}^{\nearrow}_{5kV}$, $\mathbf{Co}^{\nearrow}_{30kV}$, $\mathbf{Fe}^{\nearrow}_{5kV}$, and $\mathbf{Fe}^{\nearrow}_{5kV}$ NWs. (b) Mean atomic content of metal (Co or Fe) in the NW centre bands as a function of θ. Error bars in (b) are not drawn to improve graph readability, but would represent 3% systematic uncertainty and less than 2% random error for each point. The lines represent linear regression fits for each dataset. (c) The length of the major axis of the elliptical NW cross-section, as a function of θ. Error bars correspond to STEM image pixel size. (d) Ratio of the major and minor axes of the cross-section, as a function of θ. Error bars correspond to one standard deviation of random error. For all tested precursor gases, accelerating voltages, and beam currents, the NW metal content and cross-sectional area decrease with increasing beam movement speed.

unidirectionally magnetised and have a length-to-projected-diameter ratio greater than 5:1, $\bar{B}_y$ is indicative of the saturation induction B_0, which is an intrinsic material property. Based on modelling of the demagnetising fields, the average B_0 is expected to be from 10% to 20% greater than $\bar{B}_y$ for such NW geometries ,[64] but would require 3D characterisation to identify variations in non-ferromagnetic NW shell thickness that limit the accuracy of the micromagnetic simulations.

Magnetic Induction in Oblique NWs

Figure 7 presents magnetic imaging of NWs in $\mathbf{Co}^{\nearrow}_{5kV}$ and $\mathbf{Fe}^{\nearrow}_{30kV}$ samples as a function of growth angle θ, and by implication metal content, respectively. These samples consist of nanowires in which the metal content shows a similar dependence on θ, even though during deposition the accelerating voltage, beam current, and precursor gas were different for each sample. Figure 7a shows magnetic induction maps reconstructed from electron holography of the $\mathbf{Co}^{\nearrow}_{5kV}$ NWs deposited using a 340 pA beam current. To create magnetic induction maps, the φ_m images underwent Gaussian smoothing and the cosine was amplified (×5) to produce magnetic phase contours with $2\pi/5$ rad spacing, and colour wheels are used to show the projected $\boldsymbol{B}$ direction. Figure 7b shows line traces of φ_m as a function of θ, from which, after adjusting for variations in NW cross-sectional area, the mean B_y value in the 20 nm centre bands was calculated (Figure 7c). The error in $\bar{B}_y$ represents the combined uncertainty of projected NW thickness measurements and the standard deviation of B_y in the centre bands. It should be noted that the lowest-purity NW deposited at $\theta > 70°$ was observed to warp during STEM EELS mapping, creating a site where a magnetic domain wall regularly forms after saturating the sample. Hence, the φ_m line trace was acquired off-centre, so that it is in the middle of a uniformly magnetised region.

For comparison, Figure 7d–f show magnetic induction maps of the $\mathbf{Fe}^{\nearrow}_{30kV}$ NWs deposited using a beam current of 2800 pA (Figure 7d), line traces of φ_m as a function of θ (Figure 7e) and the calculated mean B_y value in the centre bands (Figure 7f). In both $\mathbf{Co}^{\nearrow}_{5kV}$ and $\mathbf{Fe}^{\nearrow}_{30kV}$ samples, the NWs grown at larger angles are observed to contain a lower percentage of metal atoms, and the $\bar{B}_y$ value reduction is 2 mT and 7 mT per degree of θ, respectively. As noted above, the outliers to this trend occur at $\theta \approx 0°$ in both datasets due to the stationary electron beam transmitting through the length of the NW for the entire duration of deposition, thereby altering the geometry and composition of the lower layers.

Figure 8 summarises the correlation between NW metal content and $\bar{B}_y$ measurement. The data in Figure 7c and Figure 7f are plotted with respect to the metal content in each oblique NW and are compared with the literature. The two red data points in the top right of Figure 8a correspond to the thermally annealed NWs and agree with previous works[15,28] characterising annealed Co FEBID NWs (Figure 8a, black dots and dashed lines). The underlying magnetic induction maps for annealed NWs are available in the Supporting Information Figure S15. All other blue data points correspond to $\mathbf{Co}^{\nearrow}_{5kV}$ NWs, which are not annealed, and lie outside the range of the referenced study. For FEBID NWs, $\bar{B}_y$ is smaller than 1.75 T B_0 for pure bulk Co.[23,65] For the $\mathbf{Fe}^{\nearrow}_{30kV}$ NWs, the values of $\bar{B}_y$ in Figure 8b are lower than the 2.1 T value measured for pure bulk iron.[66] $\bar{B}_y$ is lower than B_0 because it is affected by the demagnetising field and represents the thickness-average in NWs with radially varying composition, but it is indicative of the variation in effective $\boldsymbol{B}$, which scales with the percentage of metal atoms in the material. Overall, the $\boldsymbol{B}$ field created in ferromagnetic NWs is affected by growth angle due to changes in elemental composition.

Downloaded from pubs.acs.org/aanmf6/article-pdf/9/41/19185/6874537/an6c02497.pdf by FORSCHUNGSZENTRUM JUELICH user on 16 October 2026

https://doi.org/10.1021/acsanm.6c02497
ACS Appl. Nano Mater. 2026, 9, 19185–19197

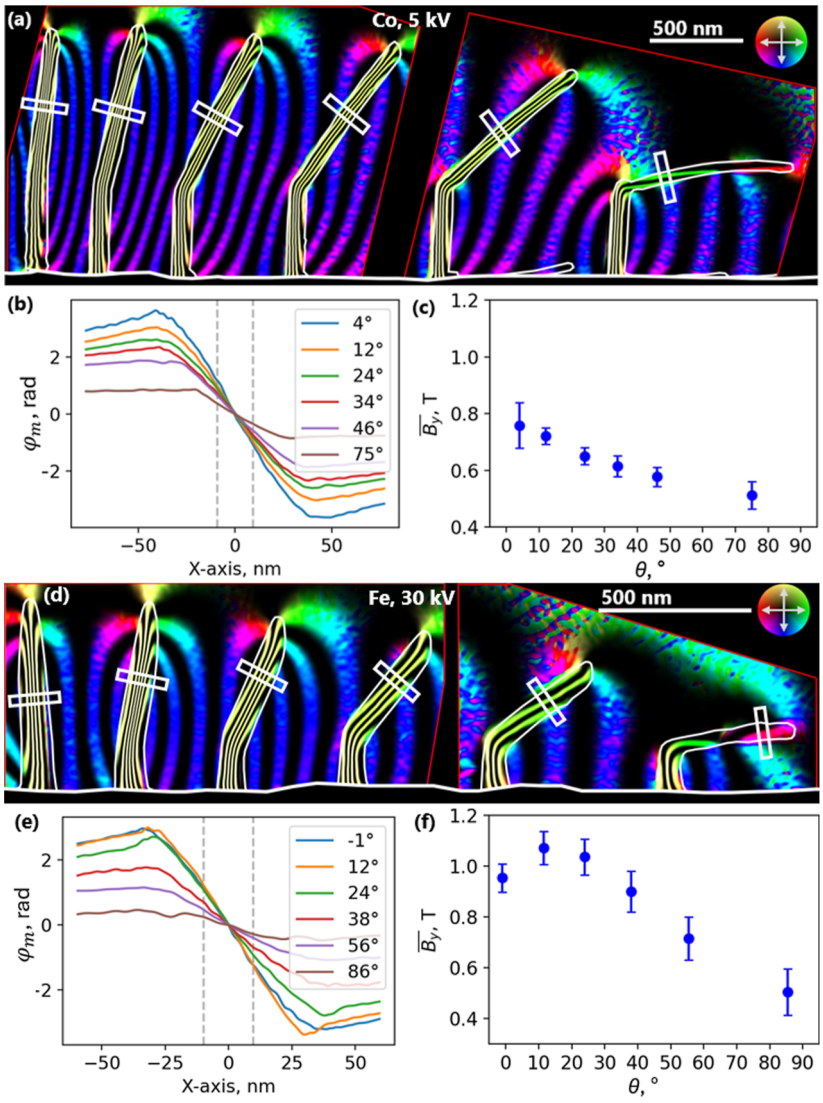


Figure 7. Magnetic characterisation of the $\mathbf{Co}^{\nearrow}_{5kV}$ (a-c) and $\mathbf{Fe}^{\nearrow}_{30kV}$ (d−f) samples. (a,d) Magnetic induction maps with contour spacings of $2\pi/5$ rad. (b,e) Line traces of φ_m are from areas corresponding to the white boxes in (a) and (d), respectively. The measured φ_m gradient is consistently smaller for higher θ. The centre bands are denoted by dashed lines. (c,f) Correlations between θ and B_y in the centre bands.

DISCUSSION

In this work, we have fabricated and analysed oblique FEBID NWs to determine improved parameters for depositing ferromagnetic material in oblique geometries. Characteristic FEBID NW variations in response to changes in deposition parameters were observed, including increases in metal content with increased electron beam current, precise focusing of the electron beam, or thermal annealing of the NWs at 350 °C for 30 min.[13,28,38] These conditions were all considered to find optimal beam currents for fabricating obliquely angled ($0° \leq \theta \leq 90°$) Co and Fe NWs at 5 kV and 30 kV accelerating voltages. In all samples, increasing the electron beam lateral movement speed characteristically increases θ, but reduces NW cross-section area, metal content, and the magnitude of $\boldsymbol{B}$. Oblique NWs that were the most symmetrical and had the highest metal content (without annealing) were deposited using the combination of the lowest tested accelerating voltage (5 kV), the highest beam current (2.8 nA), and the $Fe_2(CO)_9$ precursor.

The beam current is increased by increasing the spot size,[67] which enables more electrons to pass through the condenser aperture at the expense of beam broadening. The corresponding increase in precursor ionisation and beam-induced heating promotes deposition with higher atomic metal content, but NW diameter is increased. The highest beam current of 2.8 nA used in this study resulted in a NW diameter lower than 150 nm. Micromagnetic simulations demonstrated that, in 1 μm long Co or Fe cylinders with diameters ≤ 150 nm, $\boldsymbol{M}$ is mostly uniaxially oriented, because small diameters strengthen magnetic shape anisotropy. Hence, small-diameter NWs are investigated due to the enhanced magnetic signal associated with uniaxial magnetic configurations, which is advantageous for spintronic device applications.[2] Additionally, excessively high beam currents can lead to unpredictable NW surface topographies (Figure 4a). Especially for the $Fe_2(CO)_9$ precursor, which dissociates to $Fe(CO)_5$[20] during irradiation, FEBID can produce randomly oriented crystalline iron composed of single-crystal grains up to 1 μm in length.[21] Consequently, the maximum viable beam current is limited by the NW diameter and required growth predictability.

Downloaded from pubs.acs.org/aanmf6/article-pdf/9/41/19185/6874537/an6c02497.pdf by FORSCHUNGSZENTRUM JUELICH user on 16 October 2026

https://doi.org/10.1021/acsanm.6c02497
ACS Appl. Nano Mater. 2026, 9, 19185–19197

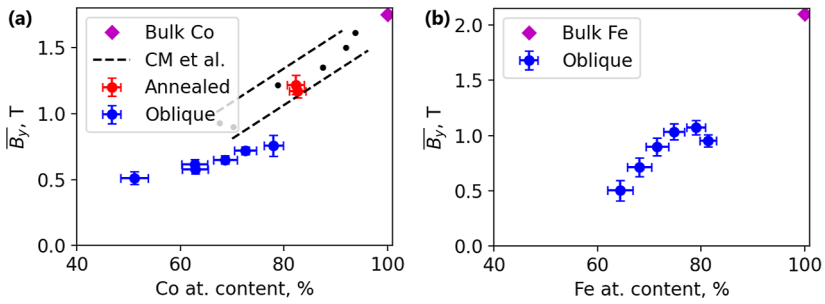


Figure 8. Correlations between NW metal content and associated magnetic properties. (a) Correlation between mean B_y and atomic Co content for FEBID NWs. As-deposited oblique NWs are shown by blue circles, annealed vertical NWs are shown by red circles, and bulk material reference values are shown by magenta diamonds. Black dots and dashed lines indicate the data and range of uncertainties in previous works ,[15] respectively. (b) Correlation between mean B_y and Fe content for oblique FEBID NWs. There is a positive correlation between metal content and the strength of magnetic induction created by the NWs. Comparison with previous works shows that the correlation is affected by structural differences within the NWs, resulting from thermal annealing and lateral beam movement. Adapted from [15], available under a CC-BY 4.0 license, copyright 2021C. Magén, J. Pablo-Navarro, and J. M. De Teresa.

The optimal electron beam acceleration voltage is often sample-specific because the electron energy affects the optical power of the SEM lenses, and alters the scattering interaction cross-sections in the NW and the substrate.[51,67] In this study, a minimum accelerating voltage of 5 kV was used, as lower voltages compromised imaging resolution and reduced the ability to achieve good focus. At 5 kV, the cross-sections of oblique NWs are circular (Figure 6d) since the interaction volume is comparable to the NW diameter and secondary electrons are generated in a localised spot.[68] At 30 kV, highly elliptical cross-sections are observed due to secondary electrons being generated along a line as the beam transmits through the NW. Additionally, the vertical growth rate in oblique NWs is larger at 5 kV compared to 30 kV (Figure 6a), whereas Table 1 shows an inverse relationship of vertical NWs growing faster at 30 kV than at 5 kV, when using high beam currents. This is attributed to the smaller interaction cross-sections of 30 kV electrons,[69] resulting in electrons imparting less energy during transmission through the sample surface. Despite sample specificity, the 0.1−5 kV range is considered advantageous for FEBID of oblique NWs due to the smaller interaction volume, where the incident beam provides an approximately point-like source of secondary electrons[13,51] and leads to more consistent deposition.

Of the tested precursors, the $Fe_2(CO)_9$ molecule is more stable than $Co_2(CO)_8$, as indicated by the higher required beam currents (Table 1) and threshold temperature for TD.[18] In Figure 6b, the elemental composition of Fe NWs, in comparison to Co, is less affected by variations in electron beam movement speed. This is attributed to improved confinement of deposition reactions, as molecules outside the immediate vicinity of the beam are less impacted by scattered electrons or conducted heat. It should be noted that other FEBID precursor gases are available ,[8] and $HCo_3Fe(CO)_{12}$ has been used to successfully deposit oblique ferromagnetic NW structures.[10]

NW arrays,[31] artificial spin ices,[10] and 3D data storage[4] prototypes can be fabricated with FEBID. Achieving uniform composition throughout these structures is essential to ensure reproducible and reliable device performance. We have demonstrated that $>75\%$ metal content can be maintained during deposition of oblique NWs angled by $0° < \theta < 60°$, when the deposition parameters are chosen to confine the reaction volume to dimensions no larger than the NW diameter, whilst using the highest viable beam current. However, NWs grown at angles of $\theta > 60°$ from the optic axis exhibit a twofold decrease in magnetic signal ($\nabla\varphi_m$) due to their reduced NW cross-sectional area. It may be possible to correct this effect by increasing the NW diameter in associated CAD modelling software.[9] The lowest observed decrease in metal at. content was, on average, $(0.11 \pm 0.05)\%$ per degree of θ. Better material uniformity may be achieved by investigating how precursor gas concentration affects oblique NWs, or by using accelerating voltages below 5 kV, which would require the introduction of additional sample features to enable fine focus. Alternatively, the substrate may be tilted to deposit oblique nanostructures with less lateral beam movement. Additionally, the metal content and resultant magnetic induction (Figure 8) may be increased by thermal annealing observed in vertical NWs (Figure 4), but the optimal temperature for preserving nanostructure uniformity would need to be determined. Figure 8a has shown that metal atom content measured in projection is not the only parameter affecting the magnetic induction created by NWs, and this may be investigated by characterising magnetic fields for a wider range of FEBID nanostructures. Overall, selecting deposition parameters to limit the reaction volume and use the highest viable electron beam current can improve the compositional uniformity of oblique ferromagnetic FEBID NWs, which is beneficial for the fabrication of uniform 3D nanostructures.

CONCLUSIONS

Strategies are discussed for optimising deposition parameters to improve material uniformity in 3D ferromagnetic FEBID nanostructures. This work demonstrates inherent variation in the material properties of oblique FEBID NWs deposited with a laterally moving electron beam, as compared to a stationary beam, and shows that these properties can be tuned by adjusting the deposition parameters. Higher-energy electron beams penetrate further into a material, which can delocalise the deposition reactions by irradiating a larger volume. FEBID of oblique Co NWs using a 30 kV beam reveals a reduction in cross-section area and a decrease in metal content by up to 0.4% per degree of growth angle relative to the optic axis. TEM characterisation confirms that the reduction of NW purity results in a corresponding weakening of the magnetic induction. Ensuring uniform NW composition enhances the consistency of functional 3D nanostructures fabricated with FEBID. Consequently, oblique NWs fabricated using different combinations of

Downloaded from pubs.acs.org/aanmf6/article-pdf/9/41/19185/6874537/an6c02497.pdf by FORSCHUNGSZENTRUM JUELICH user on 16 October 2026

https://doi.org/10.1021/acsanm.6c02497
ACS Appl. Nano Mater. 2026, 9, 19185–19197

SEM electron beam current, accelerating voltage, and precursor gas type were characterised to assess compositional variations. By using the deposition conditions of: 5 kV accelerating voltage; 2.8 nA beam current; and the $Fe_2(CO)_9$ precursor gas, the average decrease in NW metal content was limited to $(0.11 \pm 0.05)\%/^\circ$, and the NW cross-sectional shape was preserved for growth angles up to 60°. In summary, it was shown that metal content in oblique NWs is dependent on the growth angle, but variations in material properties can be minimised by using a precursor gas and accelerating voltage that confine the deposition reactions to an interaction volume no larger than the NW diameter.

■ ASSOCIATED CONTENT

Data Availability Statement

The data underlying this study are openly available in Enlighten at http://dx.doi.org/10.5525/gla.researchdata.2427.

Supporting Information

The Supporting Information is available free of charge at https://pubs.acs.org/doi/10.1021/acsanm.6c02497.

Supporting_information.pdf: EELS scans underlying the datapoints in Figure 6, a discussion about generating the model in Figure 3, comparison of high-loss EELS spectra from NWs of various projected thicknesses, additional plots showing correlations between NW geometry and atomic composition, micromagnetic simulations of NWs, and magnetic induction maps of vertical annealed NWs underlying calibration datapoints in Figure 8a (PDF).

■ AUTHOR INFORMATION

Corresponding Authors

Aurys Šilinga − *SUPA, School of Physics and Astronomy, University of Glasgow, Glasgow G12 8QQ, U.K.;* orcid.org/0000-0001-6124-1754; Email: a.silinga.1@research.gla.ac.uk

Trevor P. Almeida − *SUPA, School of Physics and Astronomy, University of Glasgow, Glasgow G12 8QQ, U.K.;* orcid.org/0000-0003-4683-6279; Email: Trevor.Almeida@glasgow.ac.uk

Authors

Keir L. Edgar − *SUPA, School of Physics and Astronomy, University of Glasgow, Glasgow G12 8QQ, U.K.;* orcid.org/0009-0001-8992-8168

András Kovács − *Ernst Ruska-Centre for Microscopy and Spectroscopy with Electrons, Forschungszentrum Jülich, 52425 Jülich, Germany;* orcid.org/0000-0001-8485-991X

Stephen McVitie − *SUPA, School of Physics and Astronomy, University of Glasgow, Glasgow G12 8QQ, U.K.;* orcid.org/0000-0003-4511-6413

Rafal E. Dunin-Borkowski − *Ernst Ruska-Centre for Microscopy and Spectroscopy with Electrons, Forschungszentrum Jülich, 52425 Jülich, Germany;* orcid.org/0000-0001-8082-0647

Kayla Fallon − *SUPA, School of Physics and Astronomy, University of Glasgow, Glasgow G12 8QQ, U.K.;* orcid.org/0009-0003-8176-3615

Complete contact information is available at: https://pubs.acs.org/doi/10.1021/acsanm.6c02497

Notes

The authors declare no competing financial interest.

■ ACKNOWLEDGMENTS

The authors acknowledge funding from the Engineering and Physical Science Research Council (Grant No. EP/W524359/1, EP/X025632/1), the European Research Council under the European Union's Horizon 2020 Research and Innovation Programme (Grant No. 856538, project "3D MAGiC"), the Deutsche Forschungsgemeinschaft (Project-ID 405553726 TRR270), and a Helmholtz fellowship. Aurys Šilinga thanks Fred Rendell-Bhatti and Wyn Williams for constructive discussions.

■ REFERENCES

(1) Nikonov, D. E.; Bourianoff, G. I.; Gargini, P. A. Power Dissipation in Spintronic Devices Out of Thermodynamic Equilibrium. *J. Supercond. Novel Magn.* **2006**, *19*, 497−513.

(2) Parkin, S. S. P.; Hayashi, M.; Thomas, L. Magnetic Domain-Wall Racetrack Memory. *Science* **2008**, *320*, 190−194.

(3) Ellis, M. O. A.; Welbourne, A.; Kyle, S. J.; Fry, P. W.; Allwood, D. A.; Hayward, T. J.; Vasilaki, E. Machine learning using magnetic stochastic synapses. *Neuromorph. Comput. Eng.* **2023**, *3*, 021001.

(4) Gu, K.; Guan, Y.; Hazra, B. K.; Deniz, H.; Migliorini, A.; Zhang, W.; Parkin, S. S. P. Three-dimensional racetrack memory devices designed from freestanding magnetic heterostructures. *Nat. Nanotechnol.* **2022**, *17*, 1065−1071.

(5) Streubel, R.; Fischer, P.; Kronast, F.; Kravchuk, V. P.; Sheka, D. D.; Gaididei, Y.; Schmidt, O. G.; Makarov, D. Magnetism in curved geometries. *J. Phys. D: Appl. Phys.* **2016**, *49*, 363001.

(6) Hertel, R. Curvature-induced magnetochirality. In *Spin*; World Scientific Publishing Company, 2013; Vol. *3*, p 1340009.

(7) Fernández-Pacheco, A.; Skoric, L.; De Teresa, J. M.; Pablo-Navarro, J.; Huth, M.; Dobrovolskiy, O. V. Writing 3D Nanomagnets Using Focused Electron Beams. *Materials* **2020**, *13*, 3774.

(8) De Teresa, J. M.; Fernández-Pacheco, A.; Córdoba, R.; Serrano-Ramón, L.; Sangiao, S.; Ibarra, M. R. Review of magnetic nanostructures grown by focused electron beam induced deposition (FEBID). *J. Phys. D: Appl. Phys.* **2016**, *49*, 243003.

(9) Skoric, L.; Sanz-Hernández, D.; Meng, F.; Donnelly, C.; Merino-Aceituno, S.; Fernández-Pacheco, A. Layer-by-Layer Growth of Complex-Shaped Three-Dimensional Nanostructures with Focused Electron Beams. *Nano Lett.* **2020**, *20*, 184−191.

(10) Keller, L.; Al Mamoori, M. K. I.; Pieper, J.; Gspan, C.; Stockem, I.; Schröder, C.; Barth, S.; Winkler, R.; Plank, H.; Pohlit, M.; Müller, J.; Huth, M. Direct-write of free-form building blocks for artificial magnetic 3D lattices. *Sci. Rep.* **2018**, *8*, 6160.

(11) Reisecker, V.; Winkler, R.; Plank, H. A Review on Direct-Write Nanoprinting of Functional 3D Structures with Focused Electron Beams. *Adv. Funct. Mater.* **2024**, *34*, 2407567.

(12) Utke, I.; Swiderek, P.; Höflich, K.; Madajska, K.; Jurczyk, J.; Martinović, P.; Szymańska, I. B. Coordination and organometallic precursors of group 10 and 11: Focused electron beam induced deposition of metals and insight gained from chemical vapour deposition, atomic layer deposition, and fundamental surface and gas phase studies. *Coord. Chem. Rev.* **2022**, *458*, 213851.

(13) Córdoba, R.; Sharma, N.; Kölling, S.; Koenraad, P. M.; Koopmans, B. High-purity 3D nano-objects grown by focused-electron-beam induced deposition. *Nanotechnology* **2016**, *27*, 355301.

(14) Botman, A.; Mulders, J. J. L.; Hagen, C. W. Creating pure nanostructures from electron-beam-induced deposition using

Downloaded from pubs.acs.org/aanmf6/article-pdf/9/41/19185/6874537/an6c02497.pdf by FORSCHUNGSZENTRUM JUELICH user on 16 October 2026

purification techniques: a technology perspective. *Nanotechnology* **2009**, *20*, 372001.
(15) Magén, C.; Pablo-Navarro, J.; De Teresa, J. M. Focused-Electron-Beam Engineering of 3D Magnetic Nanowires. *Nanomaterials* **2021**, *11*, 402.
(16) Muthukumar, K.; Jeschke, H. O.; Valentí, R.; Begun, E.; Schwenk, J.; Porrati, F.; Huth, M. Spontaneous dissociation of Co2(CO)8 and autocatalytic growth of Co on SiO2: A combined experimental and theoretical investigation. *Beilstein J. Nanotechnol.* **2012**, *3*, 546−555.
(17) Winters, R. E.; Kiser, R. W. Ions Produced by Electron Impact with the Dimetallic Carbonyls of Cobalt and Manganese1. *J. Phys. Chem.* **1965**, *69*, 1618−1622.
(18) Connor, J. A.; Skinner, H. A.; Virmani, Y. High temperature microcalorimetric studies of the thermal decomposition and iodination of polynuclear carbonyls of Fe, Co, Ru, Rh, Re, Os and Ir. *Faraday Symp. Chem. Soc.* **1973**, *8*, 18−28.
(19) Markin, E. M.; Sugawara, K.-i. Energy-Resolved Collision-Induced Dissociation of $Fe_2(CO)_y$+ (y = 1-9). *J. Phys. Chem. A* **2000**, *104*, 1416−1422.
(20) Bertini, L.; Greco, C.; De Gioia, L.; Fantucci, P. Time-Dependent Density Functional Theory Study of Fe2(CO)9 Low-Lying Electronic Excited States. *J. Phys. Chem. A* **2006**, *110*, 12900−12907.
(21) Hochleitner, G.; Wanzenboeck, H. D.; Bertagnolli, E. Electron beam induced deposition of iron nanostructures. *J. Vac. Sci. Technol. B* **2008**, *26*, 939−944.
(22) Pablo-Navarro, J.; Sanz-Hernández, D.; Magén, C.; Fernández-Pacheco, A.; de Teresa, J. M. Tuning shape, composition and magnetization of 3D cobalt nanowires grown by focused electron beam induced deposition (FEBID). *J. Phys. D: Appl. Phys.* **2017**, *50*, 18LT01.
(23) Serrano-Ramón, L.; Córdoba, R.; Rodríguez, L. A.; Magén, C.; Snoeck, E.; Gatel, C.; Serrano, I.; Ibarra, M. R.; De Teresa, J. M. Ultrasmall Functional Ferromagnetic Nanostructures Grown by Focused Electron-Beam-Induced Deposition. *ACS Nano* **2011**, *5*, 7781−7787.
(24) Begun, E.; Dobrovolskiy, O. V.; Kompaniiets, M.; Sachser, R.; Gspan, C.; Plank, H.; Huth, M. Post-growth purification of Co nanostructures prepared by focused electron beam induced deposition. *Nanotechnology* **2015**, *26*, 075301.
(25) Puydinger dos Santos, M. V.; Velo, M. F.; Domingos, R. D.; Zhang, Y.; Maeder, X.; Guerra-Nuñez, C.; Best, J. P.; Béron, F.; Pirota, K. R.; Moshkalev, S.; Diniz, J. A.; Utke, I. Annealing-Based Electrical Tuning of Cobalt−Carbon Deposits Grown by Focused-Electron-Beam-Induced Deposition. *ACS Appl. Mater. Interfaces* **2016**, *8*, 32496−32503.
(26) Almeida, T.; Mcgrouther, D.; Kovács, A.; Dunin-Borkowski, R.; Mcvitie, S. Effect of annealing on the magnetic states of FEBID-grown cobalt nanopatterns examined by off-axis electron holography. *J. Microsc.* **2020**, *279*, 217−221.
(27) Martínez-Pérez, M. J.; Pablo-Navarro, J.; Müller, B.; Kleiner, R.; Magén, C.; Koelle, D.; de Teresa, J. M.; Sesé, J. NanoSQUID Magnetometry on Individual As-grown and Annealed Co Nanowires at Variable Temperature. *Nano Lett.* **2018**, *18*, 7674−7682.
(28) Pablo-Navarro, J.; Magén, C.; de Teresa, J. M. Purified and Crystalline Three-Dimensional Electron-Beam-Induced Deposits: The Successful Case of Cobalt for High-Performance Magnetic Nanowires. *ACS Appl. Nano Mater.* **2018**, *1*, 38−46.
(29) Pablo-Navarro, J.; Winkler, R.; Haberfehlner, G.; Magén, C.; Plank, H.; De Teresa, J. M. *In situ* real-time annealing of ultrathin vertical Fe nanowires grown by focused electron beam induced deposition. *Acta Mater.* **2019**, *174*, 379−386.
(30) Shimojo, M.; Takeguchi, M.; Che, R.; Zhang, W.; Tanaka, M.; Mitsuishi, K.; Furuya, K. Effects of Heat Treatment on Electric Properties of Nanorods Formed by Electron Beam-Induced Deposition. *Jpn. J. Appl. Phys., Part 1* **2006**, *45*, 5509.
(31) Fullerton, J.; Phatak, C. Design and Control of Three-Dimensional Topological Magnetic Fields Using Interwoven Helical Nanostructures. *Nano Lett.* **2025**, *25*, 5148−5155.
(32) Sanz-Hernández, D.; Hierro-Rodriguez, A.; Donnelly, C.; Pablo-Navarro, J.; Sorrentino, A.; Pereiro, E.; Magén, C.; McVitie, S.; de Teresa, J. M.; Ferrer, S.; Fischer, P.; Fernández-Pacheco, A. Artificial Double-Helix for Geometrical Control of Magnetic Chirality. *ACS Nano* **2020**, *14*, 8084−8092.
(33) Toth, M.; Lobo, C.; Friedli, V.; Szkudlarek, A.; Utke, I. Continuum models of focused electron beam induced processing. *Beilstein J. Nanotechnol.* **2015**, *6*, 1518−1540.
(34) Sanz-Hernández, D.; Hamans, R. F.; Liao, J.-W.; Welbourne, A.; Lavrijsen, R.; Fernández-Pacheco, A. Fabrication, Detection, and Operation of a Three-Dimensional Nanomagnetic Conduit. *ACS Nano* **2017**, *11*, 11066−11073.
(35) Prosvetov, A.; Verkhovtsev, A. V.; Sushko, G.; Solov'yov, A. V. Atomistic simulation of the FEBID-driven growth of iron-based nanostructures. *Phys. Chem. Chem. Phys.* **2022**, *24*, 10807−10819.
(36) De Vera, P.; Azzolini, M.; Sushko, G.; Abril, I.; Garcia-Molina, R.; Dapor, M.; Solov'yov, I. A.; Solov'yov, A. V. Multiscale simulation of the focused electron beam induced deposition process. *Sci. Rep.* **2020**, *10*, 20827.
(37) Prosvetov, A.; Verkhovtsev, A. V.; Sushko, G.; Solov'yov, A. V. Atomistic modeling of thermal effects in focused electron beam-induced deposition of $Me_2Au(tfac)$. *Eur. Phys. J. D* **2023**, *77*, 15.
(38) Randolph, S. J.; Fowlkes, J. D.; Rack, P. D. F. Nanoscale Electron-Beam-Induced Deposition and Etching. *Crit. Rev. Solid State Mater. Sci.* **2006**, *31*, 55−89.
(39) Fernández-Pacheco, A.; De Teresa, J. M.; Córdoba, R.; Ibarra, M. R. Magnetotransport properties of high-quality cobalt nanowires grown by focused-electron-beam-induced deposition. *J. Phys. D: Appl. Phys.* **2009**, *42*, 055005.
(40) Vollnhals, F.; Drost, M.; Tu, F.; Carrasco, E.; Späth, A.; Fink, R. H.; Steinrück, H.-P.; Marbach, H. Electron-beam induced deposition and autocatalytic decomposition of Co(CO)3NO. *Beilstein J. Nanotechnol.* **2014**, *5*, 1175−1185.
(41) Utke, I.; Michler, J.; Gasser, P.; Santschi, C.; Laub, D.; Cantoni, M.; Buffat, P. t.; Jiao, C.; Hoffmann, P. Cross Section Investigations of Compositions and Sub-Structures of Tips Obtained by Focused Electron Beam Induced Deposition. *Adv. Eng. Mater.* **2005**, *7*, 323−331.
(42) Utke, I.; Hoffmann, P.; Berger, R.; Scandella, L. High-resolution magnetic Co supertips grown by a focused electron beam. *Appl. Phys. Lett.* **2002**, *80*, 4792−4794.
(43) Plank, H.; Gspan, C.; Dienstleder, M.; Kothleitner, G.; Hofer, F. The influence of beam defocus on volume growth rates for electron beam induced platinum deposition. *Nanotechnology* **2008**, *19*, 485302.
(44) Winkler, R.; Fowlkes, J. D.; Rack, P. D.; Kothleitner, G.; Plank, H. Shape evolution and growth mechanisms of 3D-printed nanowires. *Addit. Manuf.* **2021**, *46*, 102076.
(45) Wanzenboeck, H. D.; Hochleitner, G.; Mika, J.; Shawrav, M. M.; Gavagnin, M.; Bertagnolli, E. Mapping of local argon impingement on a virtual surface: an insight for gas injection during FEBID. *Appl. Phys. A* **2014**, *117*, 1749−1756.
(46) Craven, A. J.; Wilson, J. A.; Nicholson, W. A. P. A fast beam switch for controlling the intensity in electron energy loss spectrometry. *Ultramicroscopy* **2002**, *92*, 165−180.
(47) Craven, A. J.; MacKenzie, M.; McFadzean, S. In *EMC 2008 14th European Microscopy Congress 1−5 September 2008*; Luysberg, M.; Tillmann, K.; Weirich, T., Eds., Springer: Aachen, Germany, 2008, pp 363−364.
(48) Lucas, G.; Burdet, P.; Cantoni, M.; Hébert, C. Multivariate statistical analysis as a tool for the segmentation of 3D spectral data. *Micron* **2013**, *52−53*, 49−56.
(49) Scott, J.; Thomas, P. J.; MacKenzie, M.; McFadzean, S.; Wilbrink, J.; Craven, A. J.; Nicholson, W. A. P. Near-simultaneous dual energy range EELS spectrum imaging. *Ultramicroscopy* **2008**, *108*, 1586−1594.
(50) Williams, D. B.; Carter, C. B.. In *Transmission Electron Microscopy: A Textbook for Materials Science*; Williams, D. B., Carter, C. B., Eds.; Springer US: Boston, MA, 2009; pp 715−739.

Downloaded from pubs.acs.org/aanmf6/article-pdf/9/41/19185/6874537/an6c02497.pdf by FORSCHUNGSZENTRUM JUELICH user on 16 October 2026

(51) Castillo-Rico, L. R.; Flores-Mancera, M. A.; Massillon-JL, G. Stopping power and CSDA range of electrons in liquid water, LiF, CaF_2, and Al_2O_3 from the energy gap up to 433 keV. *Nucl. Instrum. Methods Phys. Res., Sect. B* **2021**, *502*, 189−197.
(52) Töberg, S.; Reithmeier, E. Quantitative 3D Reconstruction from Scanning Electron Microscope Images Based on Affine Camera Models. *Sensors* **2020**, *20*, 3598.
(53) Dunin-Borkowski, R. E.; Kovács, A.; Kasama, T.; McCartney, M. R.; Smith, D. J.. In *Springer Handbook of Microscopy*; Hawkes, P. W., Spence, J. C. H., Eds.; Springer International Publishing: Cham, 2019; pp 767−818.
(54) Völkl, E.; Allard, L. F.; Frost, B. A software package for the processing and reconstruction of electron holograms. *J. Microsc.* **1995**, *180*, 39−50.
(55) Boureau, V.; McLeod, R.; Mayall, B.; Cooper, D. Off-axis electron holography combining summation of hologram series with double-exposure phase-shifting: Theory and application. *Ultramicroscopy* **2018**, *193*, 52−63.
(56) Mitchell, D. R. G.; Schaffer, B. Scripting-customised microscopy tools for Digital Micrograph. *Ultramicroscopy* **2005**, *103*, 319−332.
(57) Aharonov, Y.; Bohm, D. Significance of Electromagnetic Potentials in the Quantum Theory. *Phys. Rev.* **1959**, *115*, 485−491.
(58) Burbridge, D. J.; Gordeev, S. N. Proximity effects in free-standing EBID structures. *Nanotechnology* **2009**, *20*, 285308.
(59) Vansteenkiste, A.; Leliaert, J.; Dvornik, M.; Helsen, M.; Garcia-Sanchez, F.; Van Waeyenberge, B. The design and verification of MuMax3. *AIP Adv.* **2014**, *4*, 107133.
(60) Joos, J. J.; Bassirian, P.; Gypens, P.; Mulkers, J.; Litzius, K.; Van Waeyenberge, B.; Leliaert, J. Tutorial: Simulating modern magnetic material systems in mumax3. *J. Appl. Phys.* **2023**, *134*, 171101.
(61) Donnelly, C.; Hierro-Rodríguez, A.; Abert, C.; Witte, K.; Skoric, L.; Sanz-Hernández, D.; Finizio, S.; Meng, F.; McVitie, S.; Raabe, J.; Suess, D.; Cowburn, R.; Fernández-Pacheco, A. Complex free-space magnetic field textures induced by three-dimensional magnetic nanostructures. *Nat. Nanotechnol.* **2022**, *17*, 136−142.
(62) Šilinga, A.; Kovács, A.; McVitie, S.; Dunin-Borkowski, R. E.; Fallon, K.; Almeida, T. P. Model-Based Iterative Reconstruction of Three-Dimensional Magnetization in a Nanowire Structure Using Electron Holographic Vector Field Tomography. *Microsc. Microanal.* **2025**, *31*, ozaf043.
(63) Rodríguez, L. A.; Deen, L.; Córdoba, R.; Magén, C.; Snoeck, E.; Koopmans, B.; De Teresa, J. M. Influence of the shape and surface oxidation in the magnetization reversal of thin iron nanowires grown by focused electron beam induced deposition. *Beilstein J. Nanotechnol.* **2015**, *6*, 1319−1331.
(64) Akhtari-Zavareh, A.; De Graef, M.; Kavanagh, K. L. Magnetic phase shift reconstruction for uniformly magnetized nanowires. *Ultramicroscopy* **2017**, *172*, 10−16.
(65) Snoeck, E.; Dunin-Borkowski, R. E.; Dumestre, F.; Renaud, P.; Amiens, C.; Chaudret, B.; Zurcher, P. Quantitative magnetization measurements on nanometer ferromagnetic cobalt wires using electron holography. *Appl. Phys. Lett.* **2003**, *82*, 88−90.
(66) Crangle, J.; Goodman, G. M. The magnetization of pure iron and nickel. *Proc. R. Soc. A* **1971**, *321*, 477−491.
(67) Williams, D. B.; Carter, C. B.. In *Transmission Electron Microscopy: A Textbook for Materials Science*; Williams, D. B., Carter, C. B., Eds.; Springer US: Boston, MA, 2009; pp 91−114.
(68) Joy, D. C.; Joy, C. S. Low voltage scanning electron microscopy. *Micron* **1996**, *27*, 247−263.
(69) Ashley, J. C.; Tung, C. J.; Ritchie, R. H.; Anderson, V. E. Calculations of mean free paths and stopping powers of low energy electrons (<10 keV) in solids using a statistical model. *IEEE Trans. Nucl. Sci.* **1976**, *23*, 1833−1837.

Downloaded from pubs.acs.org/aanmf6/article-pdf/9/41/19185/6874537o/an6c02497.pdf by FORSCHUNGSZENTRUM JUELICH user on 16 October 2026

https://doi.org/10.1021/acsanm.6c02497
ACS Appl. Nano Mater. 2026, 9, 19185−19197